Dipendra K. Roy,[1] Rajiv Tiwari[1]

Experimental identification of rotating and stationary damping in a cracked rotor system with an offset disc

In the rotor system, depending upon the ratio of rotating (internal) damping and stationary (external) damping, above the critical speed may develop instability regions. The crack adds to the rotating damping due to the rubbing action between two faces of a breathing crack. Therefore, there is a need to estimate the rotating damping and other system parameters based on experimental investigation. This paper deals with a physical model based an experimental identification of the rotating and stationary damping, unbalance, and crack additive stiffness in a cracked rotor system. The model of the breathing crack is considered as of a switching force function, which gives an excitation in multiple harmonics and leads to rotor whirls in the forward and backward directions. According to the rotor system model considered, equations of motion have been derived, and it is converted into the frequency domain for developing the estimation equation. To validate the methodology in an experimental setup, the measured time domain responses are converted into frequency domain and are utilized in the developed identification algorithm to estimate the rotor parameters. The identified parameters through the experimental data are used in the analytical rotor model to generate responses and to compare them with experimental responses.

1. Introduction

Rotating machinery operating above critical speeds requires careful study of parameters responsible for instability in the rotor to ensure the safety of personnel and machinery. Instability may occur because of more than one causes, and the rotating (internal) damping is one of the important parameters. An accurate estima-

---

✉ R. Tiwari, e-mail: rtiwari@iitg.ac.in

[1] Department of Mechanical Engineering, Indian Institute of Technology Guwahati, Guwahati – 781039, India.

tion of the rotor physical parameters through model-based identification procedure is significant. This is because these parameters can be used in analytical models to study rotor behavior to investigate instability regions. Cracks in rotor provide not only local flexibility near the crack location but also provide rotating damping due to opening and closure of the crack during rotation of the shaft, which leads to rubbing of crack faces and stress concentration at crack front. For a fully open crack condition, the stress concentration is higher, and the rubbing is negligible. During breathing of the crack, the stress concentration is lower and the rubbing is greater, whereas during the closure of the crack both will be negligible. Modeling of the rotating damping is difficult and needs estimate from rotor responses for accurate prediction in a rotor system [1].

Limited attempts have been made in the literature towards the development of procedures for the experimental estimation of rotating damping. Most of the studies focused on the instability analysis based on rotor system model owing to assumed internal damping in a possible range [2] elaborated the regions of rotor spin speed stability according to changes of whirl modes by changing the condition of internal damping [3] and [4] illustrated the forward and backward whirls analysis using Timoshenko beam theory, and study the effect of the internal and hysteretic damping to find the region of stability. They also considered the gyroscopic couple in a rotor system along with translational and rotary inertia [5] worked on the stability analysis of the rotating system based on the Timoshenko beam model considering the hysteretic damping and external damping [6] investigated the effect of hysteretic damping at the critical, subcritical, and supercritical speeds of a rotor system based on the direction of rotation considering the forward and backward whirling. Dynamic instability in a rotor system was studied by [7] and [8] based on random variations of the rotating damping. The stability analysis in a rotor system with combined consideration of the dry friction damping and the viscous internal damping was studied by [9]. Based on Euler-Bernoulli beam theory in the rotor system including the effect of rotary and translational inertia along with gyroscopic moment on the disc, [10] gave detail discussion on the estimation of the external and hysteretic damping. [11] presented a modal analysis of a rotor system and showed the effect of internal damping on the rotor instability in the presence of forces due to fluid film (external damping) from journal bearings. The stability limit speed was found to reduce owing to consideration of the shaft material (internal) damping effect.

Many authors have proposed regression-based full spectrum analysis for the identification of several rotor fault parameters. Most of them identified rotor parameters, such as the crack, residual unbalance, viscous (external) damping [12] elaborated the use of full spectrum for detection of malfunctions in the rotating machinery. The vibration caused by faults during rotation of the rotor may produce extra (or multiple) harmonic components. Hence, it includes the forward and backward whirls in the rotor orbital motion. The identification of the whirls conveys the sense of rotation concerning the spinning direction, and illustration

of what is possible based on the full-spectrum plot [13] elaborated the estimation of rotor-bearing parameters, such as the residual unbalance and bearing dynamic parameters, through the model-based method for two-degree-of-freedom of the rotor system.

The crack identification has been illustrated by many authors, which includes other parameters such as unbalance, external damping, misalignment, etc. [14] presented rotor-bearing vibrations of the system with a transverse crack opening and closure behavior of the rotor shaft. [15] worked on the response of a dynamic system of a Laval rotor with the unbalance and the shaft with a transverse crack [16] and [17] illustrated the estimation of the crack size and its location in a cracked shaft based on the finite element method. [18] and [19] described the switching crack force model in a transverse cracked shaft for the identification of parameters, such as the additive crack stiffness, viscous damping, and unbalance based regression matrix method. They considered the full spectrum analysis in the estimation of parameters, such as switching crack function with multi-harmonic components, which produced forward and backward whirls. [20, 21] extended the identification of crack parameters with an offset disc, which produces both transverse and rotary inertia along with the gyroscopic effect in a Jeffcott rotor model [22] presented a model-based methodology to identify the internal and external damping, additive stiffness, and residual unbalance in a cracked rotor system with an offset disc. However, the identification procedure was illustrated through numerical examples only.

As per the literature survey, it has been found that most of the research works focused are related to the identification of internal damping or identification of crack parameters, separately, along with other rotor parameters. However, a limited study on the experimental identification has been established based on the combined effect of a crack along with internal damping, which is most important for the practical purpose. In fact, due to instability, the crack would grow, and it will have more rotating damping and that will further reduce the instability threshold. Therefore, in the present work, the identification of the internal damping owing to the rotor crack has been attempted experimentally. The procedure is based on physical model-based regression and by utilizing the experimental full spectrum responses. The crack is modeled based on a switching function through Fourier series expansion. Dynamic condensation was used to eliminate transverse rotational displacements from EOMs (equation of motion) since such displacements are challenging to measure accurately. The full spectrum is obtained through FFT, and it requires the phase correction with respect to a reference signal with multiple harmonics. EOMs in frequency domain is used to develop identification procedure from different harmonics of responses for estimation of unknown rotor parameters, such as the rotating damping, stationary damping, unbalance, and crack stiffness. The identification procedure has been tested for its effectiveness and consistency with full spectrum responses for different combined spin speeds.

2. Modeling and identification in a cracked rotor system

This section illustrates the derivation of EOMs of a cracked rotor with an offset disc, and it is utilized in the experimental identification of rotor system fault parameters. A rotor shaft is considered with a fatigue crack that introduces the internal damping owing to rubbing of crack faces, and an offset disc gives gyroscopic moments. It also includes other parameters, such as the stationary viscous damping in bearing and unbalance owing to a manufacturing defect. For crack modeling, the switching crack function is assumed as a periodic function. Fig. 1 shows the deflected cracked shaft with an offset disc. The supports at both the ends of the rotor is assumed as a rigid in transverse translational directions, which allow only the transverse rotational motion of the shaft. Point O represents the origin of axis system, axially located at the disc on the axis passing through both end bearings. The bearing axis is represented by z-axis and x-axis is considered in the vertical (downward) direction or towards the gravity force. Due to the static force mg, it produces an initial static deflection of the disc as u_{x0} and angular displacement due to tilting of the disc as ϕ_{y0}. The rotor modeling and generation of responses has been described now.
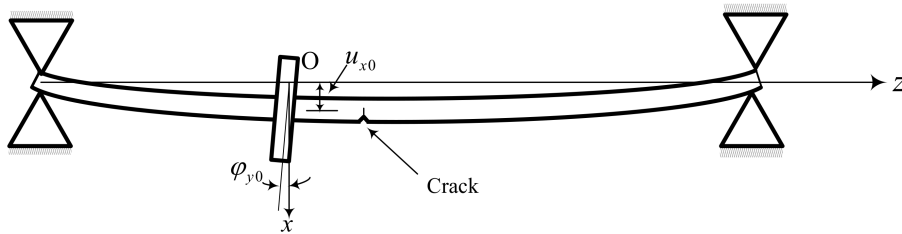

Fig. 1. Jeffcott rotor with an offset disc in the presence of a transverse crack in static condition

2.1. Model-based equations of motion

The fatigue crack in the rotor shaft results in a decrease in the local stiffness, and correspondingly the natural frequency also decreases [14, 15]. Fig. 2 depicts the motion of the disc in the stationary coordinate system (x, y) and the rotating co-ordinate axes (ξ, η). The crack front is considered perpendicular to the ξ direction. The translational disc displacements are shown in Fig. 2. Herein, ω is the shaft spin speed, t is the time instant, e is the disc eccentricity (which is the distance between the point C denoting the geometric center and G denoting the center of gravity of the disc). The angle between the unbalance (direction of e) and the direction perpendicular to the crack front (i.e., ξ axis direction) is the phase angle of unbalance and it is denoted by ϕ. Forces owing to the rotating (internal) damping (c_H), stationary (external) damping (c_E) and the gravity are shown in Fig. 2a. The tilting angles of the disc φ_{y0}, φ_y and φ_x are shown in Fig. 2b,2c. The equations of
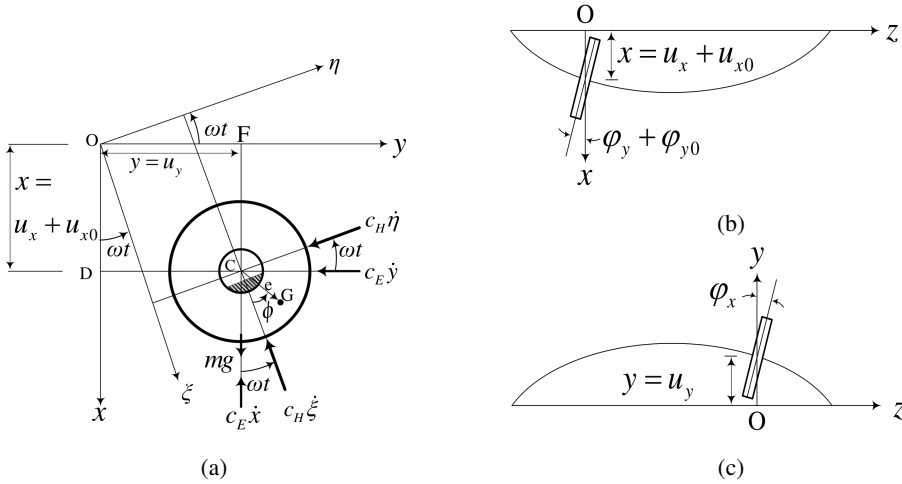
Fig. 2. Disc motion (a) in the fixed and rotating frame of references in presence various forces
(damping, disc-weight and unbalance) (b) in x-z plane, (c) in y-z plane

motion with internal damping in the presence of a transverse fatigue crack in an offset disc rotor system, including of unbalance force, is given as [22]

$$\mathbf{M}\ddot{\mathbf{q}}_v + (\mathbf{C}_E + \mathbf{C}_H - \omega\mathbf{G})\,\dot{\mathbf{q}}_v + (\omega\mathbf{C}_{1H} + \mathbf{K})\,\mathbf{q}_v = \mathbf{f}_{cr}(t) - \omega\mathbf{C}_{1H}\mathbf{q}_0 + \mathbf{f}_{unb}(t) \quad (1)$$

where $\mathbf{M}$, $\mathbf{K}$, $\mathbf{G}$, and $\mathbf{C}_E$ are the mass, stiffness, gyroscopic, and external damping matrices, respectively. Here $\mathbf{C}_H$ is symmetric matrix whereas $\mathbf{C}_{1H}$ is skew-symmetric matrix and both contain the rotating damping C_H. Also, $\mathbf{f}_{cr}$ is the crack force vector owing to the local flexibility, $\mathbf{f}_{st}$ is the static force vector due to weight of the disc, $\mathbf{f}_{unb}$ is the unbalanced force vector, $\mathbf{q}_v$ is the disc displacement vector and its first and second-time derivatives are illustrated as $\dot{\mathbf{q}}_v$ and $\ddot{\mathbf{q}}_v$, respectively. Details of the matrices and vectors are provided in Appendix A (Equation (A.1)). Equation (1) in the complex form can be expressed as

$$\bar{\mathbf{M}}\ddot{\mathbf{v}} + \left(\bar{\mathbf{C}} + \bar{\mathbf{C}}_H - j\omega\bar{\mathbf{G}}\right)\dot{\mathbf{v}} + \left(\bar{\mathbf{K}} - j\omega\bar{\mathbf{C}}_H\right)\mathbf{v} = \bar{\mathbf{f}}_{cr}(t) + \bar{\mathbf{f}}_{unb}(t) + j\omega c_H \begin{Bmatrix} u_{x0} \\ 0 \end{Bmatrix} \quad (2)$$

with

$$r = u_x + ju_y, \quad \varphi = \varphi_y + j\varphi_x, \quad \left(-I_p\omega\dot{\varphi}_x\right) + j\left(I_p\omega\dot{\varphi}_y\right) = jI_p\omega\dot{\varphi},$$

$$\omega c_H u_y - j\omega c_H u_x = -j\omega c_H r, \quad u_{x0} + ju_{y0} = r_0 e^{j\theta},$$

$$\bar{\mathbf{M}} = \begin{bmatrix} m & 0 \\ 0 & I_d \end{bmatrix}, \quad \bar{\mathbf{C}} = \begin{bmatrix} c_E & 0 \\ 0 & 0 \end{bmatrix}, \quad \bar{\mathbf{C}}_H = \begin{bmatrix} c_H & 0 \\ 0 & 0 \end{bmatrix}, \quad \bar{\mathbf{G}} = \begin{bmatrix} 0 & 0 \\ 0 & -I_p \end{bmatrix},$$

$$\bar{\mathbf{K}} = \begin{bmatrix} k_{22} & k_{23} \\ k_{32} & k_{33} \end{bmatrix}, \quad \mathbf{v}(t) = \begin{Bmatrix} r(t) \\ \varphi(t) \end{Bmatrix}, \quad \bar{\mathbf{f}}_{cr}(t) = \frac{1}{2}\sigma(t)\begin{Bmatrix} \Delta k_{22}u_{x0}\left(1 + e^{2j\omega t}\right) \\ \Delta k_{44}\varphi_{y0}\left(1 + e^{2j\omega t}\right) \end{Bmatrix}$$

and

$$\bar{\mathbf{f}}_{unb}(t) = \left\{ \begin{array}{c} me\omega^2 e^{j(\omega t + \phi)} \\ 0 \end{array} \right\},$$

$$\sigma(t) = \frac{1}{2} + \frac{2}{\pi}\cos(\omega t) - \frac{2}{3\pi}\cos 3(\omega t) + \frac{2}{5\pi}\cos(5\omega t) - \frac{2}{7\pi}\cos(7\omega t) + \cdots \quad (3)$$

Detail steps in derivation of crack force $\mathbf{f}_{cr}$ are illustrated in [20–22], $\sigma(t)$ is the switching function and its values are 0 or 1 for the crack in closed and open conditions, respectively, during rotation of the shaft. The series of multiple harmonics that appear in the crack force in Equation (3), is expressed as

$$\begin{aligned} \frac{1}{2}\sigma(t)\left(1 + e^{2j\omega t}\right) = {}& 0.25 + 0.319e^{j\omega t} + 0.25e^{2j\omega t} + 0.106e^{3j\omega t} \\ & - 0.021e^{5j\omega t} + 0.009e^{7j\omega t} + 0.106e^{-j\omega t} \\ & - 0.021e^{-3j\omega t} + 0.009e^{-5j\omega t} + \cdots \end{aligned} \quad (4)$$

The general form of Equation (4) is expressed as

$$\frac{1}{2}\sigma(t)\left(1 + e^{2j\omega t}\right) = \sum_{i=-n}^{i=n} p_i e^{ji\omega t}. \quad (5)$$

The ith term coefficient in Equation (5) is denoted by p_i, which is known as the *participation factor* of the crack force for individual harmonics. The coefficients decrease for the higher harmonics, which is independent of the crack depth in the entire range of $t_c/R < 0.5$, here t_c is the crack depth and R is the radius of the shaft. This is an assumption for the hinge model of the crack [15]. Then, the crack force taken in the following form [22]

$$\bar{\mathbf{f}}_{cr}(t) = \left\{ \begin{array}{c} \Delta k_{22} u_{x0} \\ \Delta k_{44} \varphi_{y0} \end{array} \right\} \sum_{i=-n}^{i=n} p_i e^{ji\omega t}. \quad (6)$$

Hence, the solution of the EOM in Equation (2) is taken of the following form

$$\mathbf{v}(t) = \sum_{i=-n}^{i=n} \bar{\mathbf{v}}_i e^{ji\omega t}. \quad (7)$$

Therefore, the frequency domain form of the EOM (i.e., Equation (2)) takes the following form

$$\begin{aligned} \left[-(i\omega)^2 \begin{bmatrix} m & 0 \\ 0 & I_d \end{bmatrix} + j(i\omega)\left(\begin{bmatrix} c_E & 0 \\ 0 & 0 \end{bmatrix} + \begin{bmatrix} c_H & 0 \\ 0 & 0 \end{bmatrix} + j\omega \begin{bmatrix} 0 & 0 \\ 0 & I_p \end{bmatrix} \right) \right. \\ \left. + \left(\begin{bmatrix} k_{22} & k_{23} \\ k_{32} & k_{33} \end{bmatrix} - j\omega \begin{bmatrix} c_H & 0 \\ 0 & 0 \end{bmatrix} \right) \right] \bar{\mathbf{v}}_i = \mathbf{f}_i \end{aligned} \quad (8)$$

with

$$\mathbf{f}_i = \begin{Bmatrix} \Delta k_{22} u_{x0} \\ \Delta k_{44} \varphi_{y0} \end{Bmatrix} \sum_{i=-n}^{i=n} p_i + \begin{Bmatrix} me\omega^2 e^{j\phi} \\ 0 \end{Bmatrix}_{i=1} + j\omega c_H \begin{Bmatrix} u_{x0} \\ 0 \end{Bmatrix}_{i=0}.$$

The force term $\mathbf{f}_i$ is expressed in the following form

$$\left. \begin{aligned} \mathbf{f}_0 &= \begin{Bmatrix} \Delta k_{22} u_{x0} \\ \Delta k_{44} \varphi_{y0} \end{Bmatrix} p_0 + j\omega c_H \begin{Bmatrix} u_{x0} \\ 0 \end{Bmatrix} \qquad \text{for } i = 0, \\ \mathbf{f}_1 &= \begin{Bmatrix} \Delta k_{22} u_{x0} \\ \Delta k_{44} \varphi_{y0} \end{Bmatrix} p_1 + \begin{Bmatrix} me\omega^2 e^{j\phi} \\ 0 \end{Bmatrix} \qquad \text{for } i = 1, \\ \mathbf{f}_i &= \begin{Bmatrix} \Delta k_{22} u_{x0} \\ \Delta k_{44} \varphi_{y0} \end{Bmatrix} \sum_{i=-n}^{i=n} p_i \quad \text{for } i = 2, 3, 5, 7, \cdots -1, -3, -5, \cdots \end{aligned} \right\} \tag{9}$$

In the time domain, the dynamic response of the rotor system $\mathbf{v}(t)$ is obtained by the integration of Equation (2). The multiple harmonics of the rotor system responses in the form of forward and backward whirling, $\bar{\mathbf{v}}_i$, can be estimated by the full spectrum of $\mathbf{v}(t)$. The full spectrum response is the frequency domain response, which is obtained from time domain response, and its details are illustrated in the next section.

3. Generation of full spectrum responses

Equation (7) is expressed for various forward and backward harmonics 'i', in the following form

$$\begin{aligned} \mathbf{v}(t) = \bar{\mathbf{v}}_0 &+ \bar{\mathbf{v}}_1 e^{j\omega t} + \bar{\mathbf{v}}_2 e^{2j\omega t} + \bar{\mathbf{v}}_3 e^{3j\omega t} + \bar{\mathbf{v}}_5 e^{5j\omega t} \\ &+ \bar{\mathbf{v}}_{-1} e^{-j\omega t} + \bar{\mathbf{v}}_{-3} e^{-3j\omega t} + \bar{\mathbf{v}}_{-5} e^{-5j\omega t} + \dots \end{aligned} \tag{10}$$

The appearance of various terms, $\bar{\mathbf{v}}_0, \bar{\mathbf{v}}_1, \bar{\mathbf{v}}_{-1}, \bar{\mathbf{v}}_2, \bar{\mathbf{v}}_{-2}, \dots$ in the above equation, which represents that the complex displacement can be expressed in terms of amplitude and phase corresponding to different harmonics, $\omega, -\omega, 2\omega, -2\omega,$ $\dots$, which in graphical illustration, is called the full spectrum. Two methods are illustrated in the next sub-section to extract the full spectrum from responses.

3.1. Description of regression-based full spectrum

The estimation of unknown complex displacement ($\bar{\mathbf{v}}_0, \bar{\mathbf{v}}_1, \bar{\mathbf{v}}_{-1}, \bar{\mathbf{v}}_2, \bar{\mathbf{v}}_{-2}, \dots$) is known as the full spectrum displacements, Equation (10) is expressed in the form of the regression equation (for the current case considered only up to 7th positive and up to 5th negative harmonic expressions), as

$$\mathbf{A}_{1_{n\times 9}} \bar{\mathbf{v}}_{i_{9\times 1}} = \mathbf{v}_{n\times 1}. \tag{11}$$

The details of the matrices and vectors are illustrated in Appendix A (Equation (A.2)). Equation (11) gives the estimation of the unknown complex displacements when using time domain displacement responses $\mathbf{v}(t)_{n\times 1}$ as input from experimental setup through non-contact proximity probes in two transverse orthogonal directions. Equation (11) can be expressed as

$$\bar{\mathbf{v}}_{i_{9\times 1}} = \left(\mathbf{A}_1^{\mathrm{T}}\mathbf{A}_1\right)^{-1}\mathbf{A}_1^{\mathrm{T}}\mathbf{v}(t). \tag{12}$$

Equation (12) gives an estimation of, $\bar{\mathbf{v}}_{i_{9\times 1}}$, which denotes the unknown displacement of full spectrum. For the present case, only up to 7th positive harmonics and up to 5th negative harmonics are considered. The present method requires large numbers of time domain data sets for estimation, which is time-consuming. Therefore, FFT based full spectrum estimation is illustrated in the next subsection along with the phase compensation in full spectrum.

3.2. Description of FFT-based full spectrum

The most popular tool for the conversion of time domain responses to frequency domain responses is known as FFT. The comparison of estimation through regression-based (i.e., Equation (12)) and FFT-based full spectrum of multi-harmonic response is necessary for its computational efficiency. It is observed that both of the estimation methods (i.e., FFT-based and regression-based) of the full spectrum give the amplitude same for each harmonic but phase differ. To avoid this discrepancy, a time domain signal has to be measured at the same time instants with respect to a shaft reference signal. While time domain displacement signal is selected, the focus is given on the selection of complete cycle of shaft rotation, (such as $\omega t = 2\pi n$, where n is an integer) to avoid leakage error (which gives inconsistency in both amplitude and phase while performing FFT). However, it is problematic to capture signals in the aforementioned method for all practical purposes. Adequate phase compensation can be performed to remove the ambiguity in phase, with the help of reference signal having multiple harmonics all in the same phase. The full-spectrum estimation methodology is used according to the paper [22], in which, the magnitude is represented by $|\bar{v}_i(\omega)|$, and the phase is represented by $\angle\theta_i$ for i^{th} harmonic of the response displacement with i is an integer (positive as well as negative). Herein, multiple harmonics of the reference signal, which in complex form is utilized in the analysis. The phase of ith harmonic of the reference signal is denoted by $\angle\psi_i$. The compensated full spectrum [22] is given as

$$\bar{v}_{ci} = |\bar{v}_i(\omega)|\angle(\theta_i - \psi_i) \tag{13}$$

where $\bar{v}_{ci} = R_{i_{\mathrm{Re}}} + \mathrm{j}R_{i_{\mathrm{Im}}}$ is the modified full-spectrum complex displacement.

Firstly, the estimation of system parameters is performed by both the methods described in this section, viz. the regression-based and FFT-based methods, and

are compared for the correctness and its accuracy. Before the identification of the system, it is important to eliminate rotational DOFs (degrees of freedom) from governing equations, which is illustrated in the next section.

4. Application of dynamic reduction scheme

In the present section, the dynamic reduction technique is utilized to remove rotational (owing to tilting) DOFs. An accurate experimental measurement of disc tilting (rotational DOFs) response is difficult. In Equation (8), the transverse translational and rotational displacements are present, which are referred as master DOFs and slave DOFs, respectively, and it is represented with subscripts m and s, respectively. Moreover, the crack force in the right side of Equation (8) due to rotational DOFs are ignored in the development of the transform matrix. After partition of matrices for the master and slave DOFs, it takes the following form

$$
\begin{aligned}
&\left[-(i\omega)^2 \begin{bmatrix} \mathbf{M}_{mm} & 0 \\ 0 & \mathbf{M}_{ss} \end{bmatrix} + j(i\omega)\left(\begin{bmatrix} \mathbf{C}_{mm} & \mathbf{C}_{ms} \\ \mathbf{C}_{sm} & \mathbf{C}_{ss} \end{bmatrix} - j\omega \begin{bmatrix} 0 & 0 \\ 0 & \mathbf{G}_{ss} \end{bmatrix} \right) \right. \\
&\left. + \left(\begin{bmatrix} \mathbf{K}_{mm} & \mathbf{K}_{ms} \\ \mathbf{K}_{sm} & \mathbf{K}_{ss} \end{bmatrix} - j\omega \begin{bmatrix} \mathbf{C}_{H_{mm}} & 0 \\ 0 & 0 \end{bmatrix} \right) \right] \begin{Bmatrix} \mathbf{q}_{mm} \\ \mathbf{q}_{ss} \end{Bmatrix} = \begin{Bmatrix} \mathbf{f}_i \\ \mathbf{0} \end{Bmatrix}.
\end{aligned}
\tag{14}
$$

Details of the vectors and matrices in Equation (14) are illustrated in Appendix A (Equation (A.3)). The statement of the transformation matrix, $\mathbf{T}^D$, according to the dynamic condensation is obtained as

$$
\{\mathbf{q}_{mm}\} = [I]\{\mathbf{q}_{mm}\}, \qquad \begin{Bmatrix} \mathbf{q}_{mm} \\ \mathbf{q}_{ss} \end{Bmatrix} = \mathbf{T}^D \{\mathbf{q}_{mm}\}
\tag{15}
$$

with

$$
\mathbf{T}^D = \begin{Bmatrix} \mathbf{I} \\ \mathbf{L}_i \end{Bmatrix}, \qquad \text{where} \qquad \mathbf{L}_i = \frac{-\mathbf{K}_{sm}}{\mathbf{K}_{ss} + i\omega^2 \mathbf{G}_{ss} - (i\omega)^2 \mathbf{M}_{ss}},
$$

where ω is considered as the central frequency in the range of frequency of interest. According to the transformation and with consideration of the crack force owing to rotational DOFs in Equation (14), it is expressed in the following form

$$
\begin{aligned}
&\left(\mathbf{T}^D \right)^T \left[-(i\omega)^2 \begin{bmatrix} m & 0 \\ 0 & I_d \end{bmatrix} + ij\omega \begin{bmatrix} c_E & 0 \\ 0 & 0 \end{bmatrix} + (i-1)j\omega \begin{bmatrix} c_H & 0 \\ 0 & 0 \end{bmatrix} \right. \\
&\left. + i\omega^2 \begin{bmatrix} 0 & 0 \\ 0 & -I_p \end{bmatrix} + \begin{bmatrix} k_{22} & k_{23} \\ k_{32} & k_{33} \end{bmatrix} \right] \mathbf{T}^D \mathbf{q}_{mm} = \left(\mathbf{T}^D \right)^T \left(\begin{Bmatrix} \Delta k_{22} u_{x0} \\ 0 \end{Bmatrix} \sum_{i=-n}^{i=n} p_i \right. \\
&\left. + \begin{Bmatrix} m e \omega^2 e^{j\phi} \\ 0 \end{Bmatrix}_{i=1} + j\omega c_H \begin{Bmatrix} u_{x0} \\ 0 \end{Bmatrix}_{i=0} \right).
\end{aligned}
\tag{16}
$$

According to i^{th} harmonic, $\mathbf{T}^D$ is expressed as

$$\mathbf{T}_i^D = \begin{bmatrix} 1 & 0 & t_i^d & 0 \\ 0 & 1 & 0 & t_i^d \end{bmatrix}^T, \qquad \text{where} \quad t_i^d = \frac{-k_{42}}{k_{44} - i\omega^2 I_p - (i\omega)^2 I_d}. \qquad (17)$$

The reduced EOM (Equation (16)) with the help of transfer matrices is expressed in the following form

$$\left(-(i\omega)^2 \mathbf{M}^D + ij\omega \mathbf{C}^D + (i-1)j\omega \mathbf{C}_H^D + i\omega^2 \mathbf{G}^D + \mathbf{K}^D\right) \mathbf{q}_{mm} = \mathbf{f}^D. \qquad (18)$$

On substituting Equations (A.4) through (A.9) into Equation (18) including the complex form of the displacement vector, which is assumed as $\mathbf{q}_{mm} = R_i$, we can get a single equation and is expressed as

$$\left(-(i\omega)^2 m_i + ij\omega\,(c_E) + (i-1)j\omega c_H - i\omega^2 I_p \left(t_i^d\right)^2 + k_i\right) R_i$$
$$= me\omega^2 e^{j\beta} + (\Delta k_{22} u_{x0})\, p_i + j\omega c_H u_{x0} \qquad (19)$$

with

$$m_i = \left\{ m + \left(t_i^d\right)^2 I_d \right\}, \quad k_i = \left\{ k_{22} + 2t_i^d k_{24} + \left(t_i^d\right)^2 k_{44} \right\} \quad \text{and} \quad R_i = R_{i_{\text{Re}}} + j R_{i_{\text{Im}}}.$$

5. Identification of internal damping and other rotor parameters

The description of the identification of the system parameter is presented in this section. The method is presented for the estimation of unknown rotor system parameters, such as the internal damping, external damping, additive crack stiffness, and unbalance, which are difficult to predict by theoretical modeling. Equation (8) is used to convert into a regression procedure to estimate the unknown parameters. The complex form of Equation (19) is split, as

Real terms

$$-i\omega\,(c_E)\, R_{i_{\text{Im}}} - (i-1)\omega c_H R_{i_{\text{Im}}} - m\omega^2 e_{\text{Re}} - (\Delta k_{22} u_{x0})\, p_i$$
$$= \left((i\omega)^2 m_i + i\omega^2 I_p \left(t_i^d\right)^2 - k_i\right) R_{i_{\text{Re}}} \qquad (20)$$

Similarly, imaginary terms

$$i\omega\,(c_E)\, R_{i_{\text{Re}}} + ((i-1)R_{i_{\text{Re}}} - u_{x0})\, \omega c_H - m\omega^2 e_{\text{Im}}$$
$$= \left((i\omega)^2 m_i + i\omega^2 I_p \left(t_i^d\right)^2 - k_i\right) R_{i_{\text{Im}}}. \qquad (21)$$

Equations (20) and (21) are rearranged in matrix form for the identification by using different harmonics and is expressed as

$$\mathbf{A}\,\mathbf{x} = \mathbf{b}. \qquad (22)$$

In the identification, the vector of unknown parameters is $\mathbf{x}$, and the details of the vectors and matrices, such as $\mathbf{x}$, $\mathbf{A}$ and $\mathbf{b}$ in Equation (22), are given in Appendix A (Equation (A.10) and (A.11)). For the estimation of $\mathbf{x}$, Equation (22) takes the following form

$$\mathbf{x} = \left(\mathbf{A}^T \mathbf{A} \right)^{-1} \mathbf{A}^T \mathbf{b}. \tag{23}$$

More accurate identification of the vector, $\mathbf{x}$, can be achieved by considering multiple speeds of rotor displacement data. Hence, for the combined spin speeds $\omega_1, \omega_2, \ldots, \omega_n$, Equation (22) can be written as

$$\begin{bmatrix} \mathbf{A}(\omega_1) \\ \mathbf{A}(\omega_2) \\ \vdots \\ \mathbf{A}(\omega_n) \end{bmatrix} \mathbf{x} = \begin{Bmatrix} \mathbf{b}(\omega_1) \\ \mathbf{b}(\omega_2) \\ \vdots \\ \mathbf{b}(\omega_n) \end{Bmatrix}. \tag{24}$$

Further, the expression of identity is utilized in the next section to illustrate the estimation of system parameters, experimentally, and it is used in numerical simulation for validation.

6. Experimental analysis

The transverse fatigue crack in the shaft has been generated based on three-point bending test at UTM machine at Strength of Material Laboratory, IIT Guwahati. The variation of compressive load applied on the shaft with the support span of 140 mm is from 1.8 kN to 6.0 kN at operating frequency of 10 Hz. The stress ratio utilized for this purpose is 0.3 at room temperature.
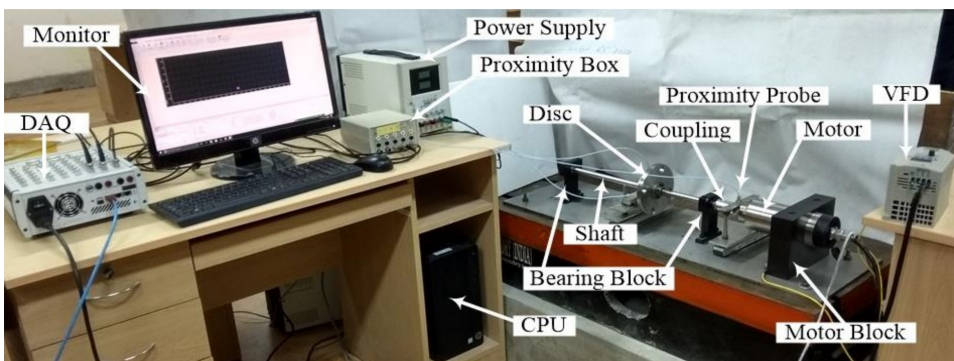

Fig. 3. Arrangement of the crack shaft experimental setup

On the motor shaft, instead of single slot (phase marker), there are two slots (phase markers) at $180°$ with some difference in size. This gives the frequency of the phase marker twice of the fundamental vibration component. However, only
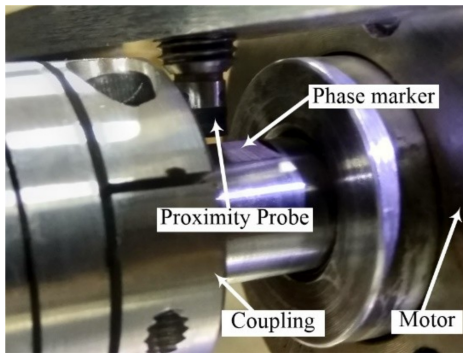
Fig. 4. Motor shaft with a slot and the sensor location
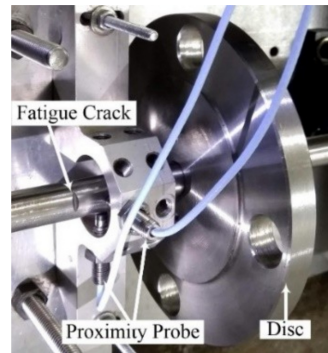for the reference signal

Fig. 5. Close view of sensor, crack
and disc

Fig. 6. Close view of the fatigue crack at the tip of the notch on the shaft

one slot is chosen as a phase marker for the reference signal. Figures 5 and 6 show the crack location near to the disc onto shaft and the close view of the crack at the notch in the shaft, respectively.

6.1. Initial observations from the test rig

Two eddy-current proximity sensors are utilized for acquiring vibrational displacements of the cracked rotor system, which are located in two orthogonal transverse directions near the offset disc, as illustrated in Fig. 5. The sensor sensitivity of the proximity sensor is 7.478 V/mm. A third sensor is utilized for the phase reference and is placed at the slot of the rigid motor shaft, so the negligible transverse displacement of the motor shaft during its rotation. An impact test in the vertical direction of the cracked rotor system was done for different shaft orientations to obtained highest and lowest natural frequencies corresponding to fully closed (healthy shaft) and fully open crack conditions.

The maximum natural frequency obtained is 65.0 Hz, when the crack was in horizontal position and direction of impact is in the vertical direction, as shown in Fig. 7. For this case, the notch effect was minimum, which was made for

the initiation of a fatigue crack. Minimum natural frequency was obtained when crack was in the downward direction and is 63.0 Hz. When the crack was in the vertical direction, the natural frequency was 64.0 Hz. Using the influence coefficient method [1], also natural frequency was obtained for intact shaft based on geometry and material properties (refer Table 1) and a comparison is shown in Table 1.

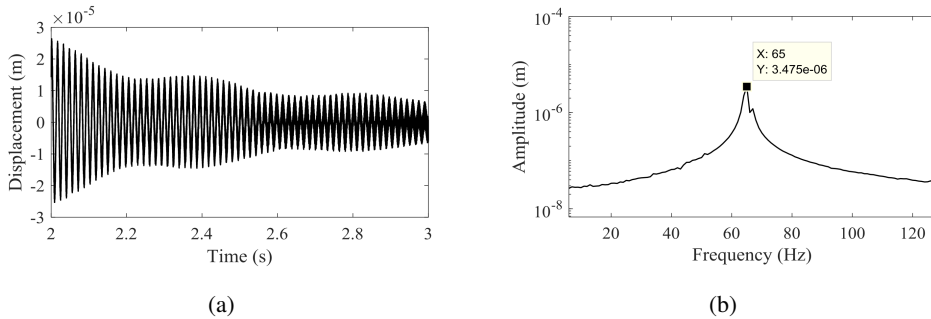(a)   (b)

Fig. 7. Free vibration response of shaft due to impulsive force with an orientation of crack is placed in the horizontal direction (a) time domain response and (b) frequency domain response

Table 1.

Rotor system parameters

Parameters	Symbol	Value	Unit
Mass of disc	m	1.8	kg
Mass moment of inertia	I_p	0.00489	kg·m^2
	I_d	0.00235	kg·m^2
Intact shaft stiffness	k_{22}	3.5056×10^5	N/m
	k_{24}	1.9671×10^4	N
	k_{44}	1.7048×10^4	Nm
Natural frequency	ω_{th}	67.9	Hz
	ω_{exp}	65.0	Hz
Shaft static deflection	u_{x0}	5.386×10^{-5}	m
Static tilting angle	φ_{y0}	-6.21×10^{-5}	rad
Length of shaft	l	0.46	m
	a	0.26	m
	b	0.20	m

A VFD-M power source unit regulated the motor speed. Measurement was taken near 3 Hz of motor speed for the slow run condition [23, 24]. The dSPACE DAQ system is utilized to store the measurement signal at a sampling frequency of 10 000 samples per second. The reference signal was utilized for acquiring displacement signals of the shaft for complete multiple shaft rotational cycles,

i.e. for $\omega t = 2\pi n$, where n is the number of complete cycles. The importance of complete cycles is given in [22] to avoid leakage error. For the slow run condition, the acquisition of complete cycles of signals is illustrated in Fig. 8.
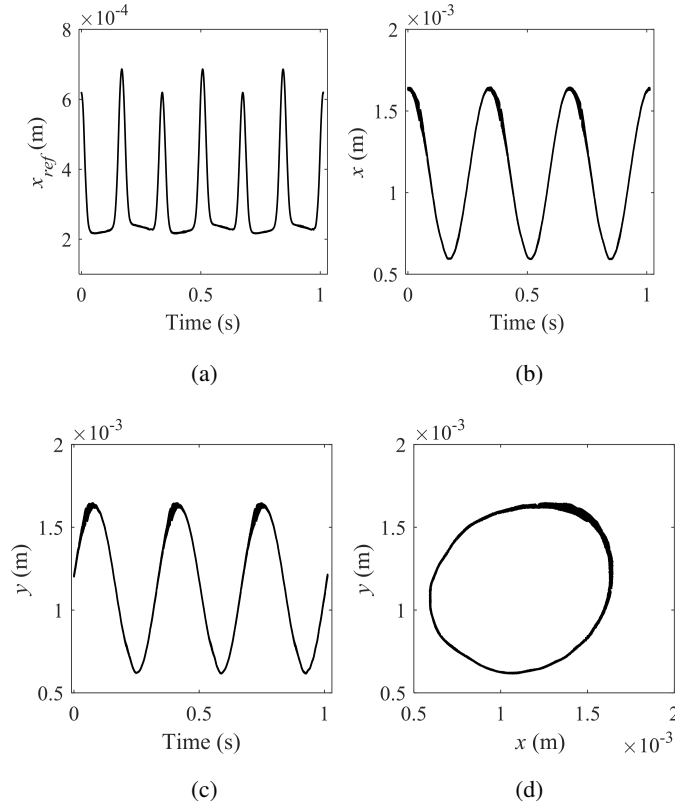

Fig. 8. Time domain response for slow roll near at 3 Hz (a) vertical direction reference signal
(x-direction) (b) vertical displacement (x-direction) (c) horizontal displacement (y-direction)
and (d) orbit plot from the vertical and horizontal displacements

Fig. 8a illustrates three complete cycles of the reference signal for 3 Hz motor speed from the vertical direction sensor. During the same time duration, displacement signals are acquired near the disc in both vertical (x-axis) and horizontal (y-axis) directions and are illustrated in Figs. 8b and 8c, respectively. Also, Fig. 8d depicts the shaft displacement orbit plot and it is seen that the origin is not inside the plot, which shows the gap between the sensors and shaft in two orthogonal directions (x and y) at the slow run condition. Since at slow run condition the dynamic force is very low, hence Fig. 8d shows only the bow and sensor gap. From Figs. 8b, 8c, 8d, it is to be noted that displacements have higher amplitudes due to bow of the shaft. Similarly, for the higher spin speeds of 20 Hz, complete cycle acquisition of signal is shown in Fig. 9.
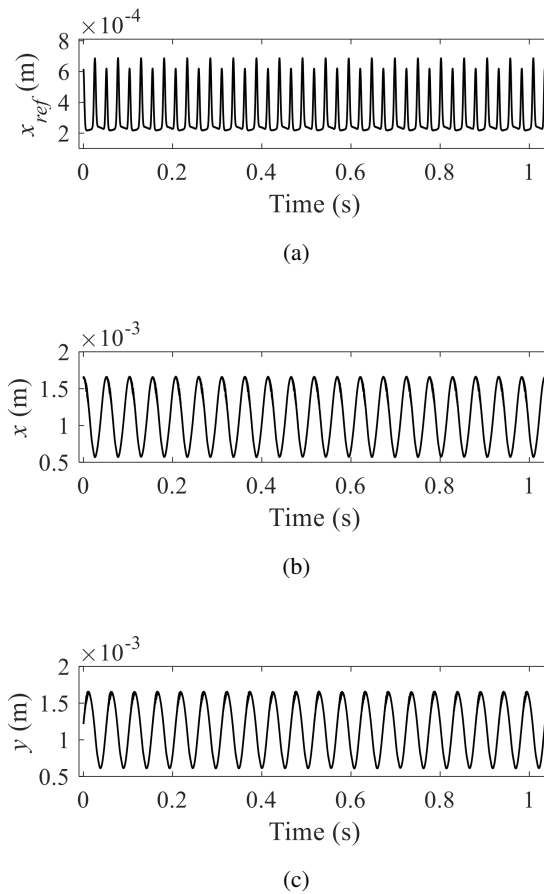
(a)

(b)

(c)

Fig. 9. Time domain response at 20 Hz (a) vertical direction reference signal (x-direction) (b) vertical displacement and (c) horizontal displacement (y-direction

Now the FFT-based full spectrum, which was earlier discussed in Section 3, is illustrated for the acquired time domain responses from the experimental setup for slow roll and higher speeds. The responses in the vertical and horizontal directions at disc location along with the reference signal are transformed in full spectrum domain, which has a form of complex numbers.

These are illustrated in Fig. 10, and Fig. 11 for 3 Hz for the slow roll condition, and 20 Hz for the higher spin speeds, respectively. Figs. 10a and 11a represent the full spectrum amplitudes with frequency both in positive and negative directions of the motor speed, and Fig. 10b and Fig. 11b represent the phase of the full spectrum corresponding to displacements near the disc. For the reference signal, Fig. 10c and Fig. 11c represent the amplitudes, and its phases are represented in Fig. 10d and Fig. 11d, respectively, for 3 Hz and 20 Hz of motor speed.
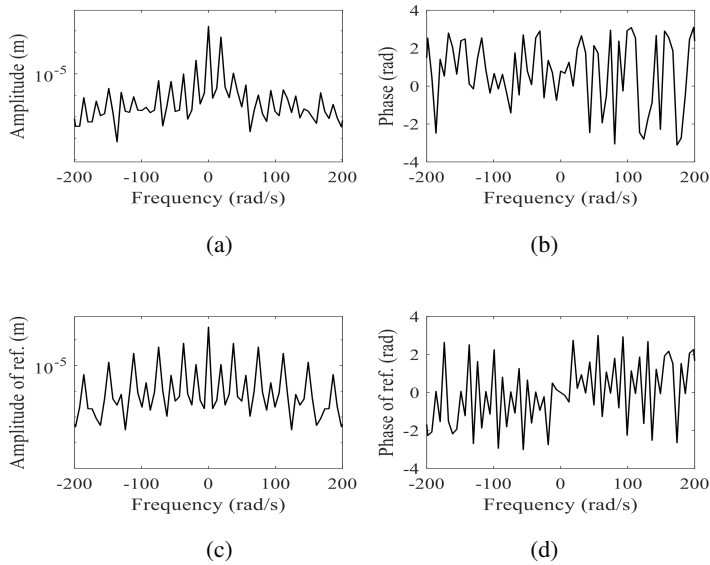
Fig. 10. Full spectrum plots for the slow roll at 3 Hz (a) amplitude of shaft displacements (b) phase of shaft displacements (c) amplitude of reference signals and (d) phase of reference signals
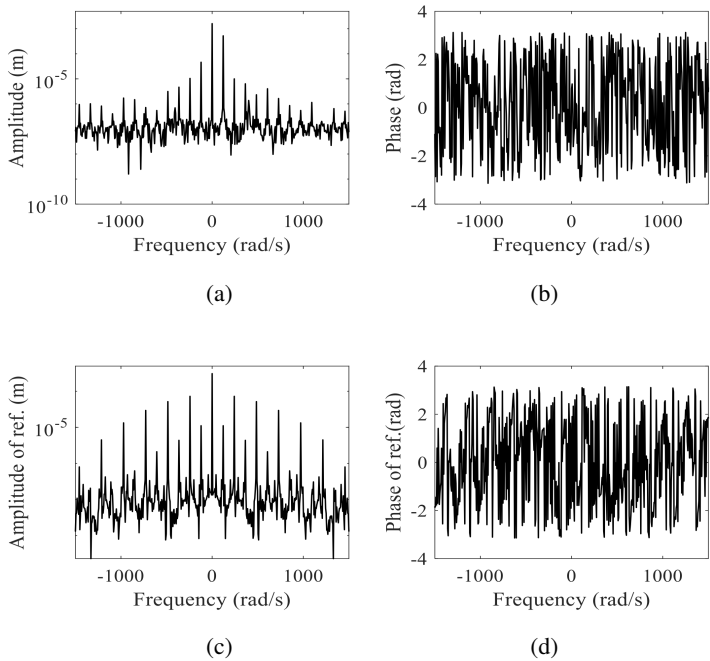

Fig. 11. Full spectrum plots for the slow roll at 3 Hz (a) amplitude of shaft displacements (b) phase of shaft displacements (c) amplitude of reference signals and (d) phase of reference signals

6.2. Comparisons of full spectra

The present section illustrates a comparison of the estimation of two full spectrum methods, i.e., regression-based and FFT-based. Amplitudes and phase angles of complex shaft displacements, and phase angles of the complex reference signal at different harmonics for the slow roll shaft speed (i.e., 3 Hz) are provided for both the first and second methods in Table 2 for comparison. Phase angles of reference signals are used for the phase correction of displacement signals and the procedure is described in the next subsection. Similarly, displacement amplitudes and phase angles at different harmonics, for higher spin speeds of 20 Hz, are provided in Table 3. It can be inferred that the variations in amplitudes are found to

Table 2.

Amplitudes, phase angles and reference phase angles at different harmonics of full spectrum for slow run rotor speed (3 Hz)

Frequency	Amplitudes		Phase angle		Reference phase angle	
	Regression $(10^{-5}$ m)	FFT $(10^{-5}$ m)	Regression (rad)	FFT (rad)	Regression (rad)	FFT (rad)
0	160.7689	160.7728	0.7931	0.7930	0	0
ω	51.3491	51.3489	−0.0022	−0.0013	2.7451	2.7457
2ω	1.0689	1.0698	1.7482	1.7547	−0.0281	−0.0262
3ω	0.3017	0.3019	1.7213	1.7320	3.0001	3.0031
5ω	0.1687	0.1675	−0.2610	−0.2588	2.9232	2.9303
7ω	0.0928	0.0929	−1.7243	−1.7245	2.6542	2.6835
$-\omega$	4.2316	4.2322	1.3574	1.3559	−2.7451	−2.7457
-3ω	0.4413	0.4397	2.7078	2.7046	−3.0002	−3.0031
-5ω	0.0268	0.0278	−0.1526	−0.1491	−2.9234	−2.9303

Table 3.

Amplitudes, phase angles and reference phase angles at different harmonics of full spectrum for the 20 Hz spin speed

Frequency	Amplitudes		Phase angle		Reference phase angle	
	Regression $(10^{-5}$ m)	FFT $(10^{-5}$ m)	Regression (rad)	FFT (rad)	Regression (rad)	FFT (rad)
0	160.6459	160.6419	0.7933	0.7933	0	0
ω	52.2777	52.2767	0.0190	0.0251	2.7966	2.8024
2ω	0.9996	0.9982	1.7815	1.7984	−0.0053	0.0068
3ω	0.6365	0.6375	1.3079	1.3296	−3.1343	−3.1163
5ω	0.4044	0.4056	−0.5920	−0.5641	−3.1129	−3.0832
7ω	0.0864	0.0871	−1.3129	−1.2764	−3.0795	−3.0409
$-\omega$	4.6157	4.6148	1.2915	1.2849	−2.7966	−2.8024
-3ω	0.4653	0.4650	−1.5999	−1.6145	3.1344	3.1163
-5ω	0.0546	0.0541	1.7239	1.6786	3.1131	3.0832

be negligible by two independent methods, whereas, the variations in phase angles become negligible only after the phase compensation.

The effect of shaft bow is nullified, as described in subsequent sections, from displacement amplitudes, and a comparison of orbit plots is also presented. Finally, the rotor system parameters are estimated.

6.3. Removing the effect of bow and sensor gap of the shaft

The removal of the bow after phase compensation is discussed in numerical simulation. It is important for the correct identification of rotor parameters that the bow effect is removed from shaft displacement signals by using the slow roll measurement of shaft displacement signals [23, 24]. To reduce the effect of bow, the complex displacement in full spectrum at slow roll of rotor speed (i.e., in vector form) for 1X harmonic is removed from the complex displacement in the full spectrum at higher rotor spin speed. When the parameters to be estimated also depend upon at the zeroth harmonic, such as due to internal damping (c_H) and the participation factor (p_0) in Equations (20) and (21), then the role of equilibrium position becomes more important as compared to the position of sensor gap removal for the actual amplitude at the 0X harmonic. Hence, for the removing of the sensor gaps with the help of full spectrum of slow roll at 0X harmonic from the full spectrum of higher rotor speed, is similar to removing of the bow effect and it is illustrated in Equation (25). However, the rest of the harmonics of the full spectrum remains the same and is expressed as

$$\underset{\substack{\text{without bow and}\\\text{sensor gap}}}{\mathbf{s}_1(t)} = \underset{\substack{\text{Experimental data}\\\text{with bow and}\\\text{sensor gap}}}{\mathbf{s}(t)} - \underbrace{\left(\left(\mathbf{R}_0 + \mathbf{R}_1 e^{j\omega t}\right)_{\text{higher spin speed}}\right)}_{\text{without phase compensation}}$$

$$+ \underbrace{\left((\mathbf{R}_0)_{\text{higher spin speed}} - (\mathbf{R}_0)_{\text{slow roll}}\right)}_{\substack{\text{removing sensor gap from equilibrium}\\\text{position after phase compensation}}} \tag{25}$$

$$+ \underbrace{\left((\mathbf{R}_1)_{\text{higher spin speed}} - (\mathbf{R}_1)_{\text{slow roll}}\right)}_{\text{removing bow after phase compensation}} e^{j\omega t}.$$

Equation (25) is used for finding out the response at higher shaft speeds after removal of the bow and sensor gaps. The corrected full spectrum amplitude and phase are utilized for the identification of rotor parameters, like the rotating damping, stationary damping, unbalance, and additive crack stiffness. The comparisons of responses with or without bow and sensor gap are discussed in the next section.

6.4. Response comparison analysis

The response of time domain orbit plots, based on Equation (25) for the rotor speed of 20 Hz, is illustrated in Fig. 12b and it is without the effect of bow and

sensor gap from equilibrium position of the rotor shaft. Displacements are reduced from the order 10^{-3} to 10^{-5} m and the origin is outside the orbit in this figure, as compared to Fig. 12a, due to bow and the effect of sensor gap. Hence, after the removal of the sensor gap, the origin comes inside the orbit as shown in Fig. 12b. Since the crack was initiated by fatigue loading, hence the actual crack propagation is not known and so the orbit is not correlating with hypothetical mathematical models in which symmetry prevails. Fig. 13 shows the full spectrum amplitude without bow and without sensor gap at the spin speed of 20 Hz rotor speed for 20 complete cycles of data. It can be observed that full spectrum plot is not symmetric due to the nature of fatigue crack.
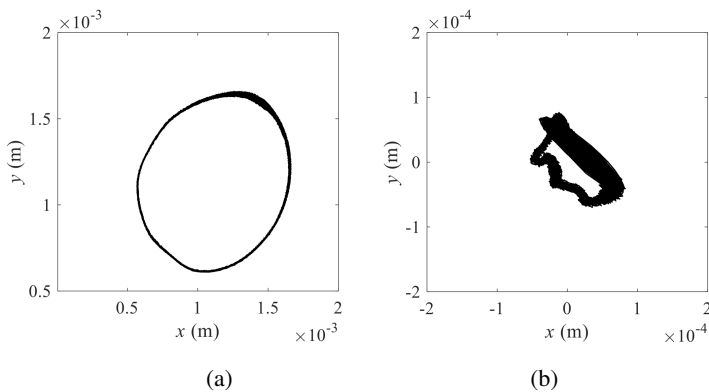

Fig. 12. Orbit plot (x vs. y) for higher spin speed at 20 Hz (a) with a bow from sensor position (b) without bow from the equilibrium position
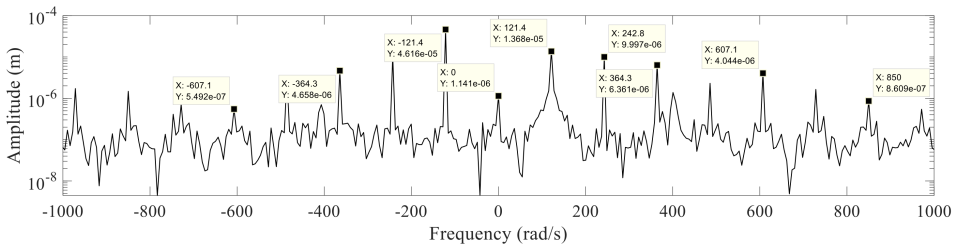

Fig. 13. Full spectrum amplitude without bow and without sensor gap at the spin speed 20 Hz rotor speed for 20 complete cycles

6.5. Estimation of rotor system parameters

The amplitudes and phases of the full spectrum displacement responses after application of the phase compensation and the removal of the bow and sensor gap through Equation (25), are utilized in the identification of rotor parameters using the regression Equation (24). The identified parameters of the cracked rotor system are

summarized in Table 4. For different combined speeds, such as the first combined speeds for 15 Hz, 16 Hz, 17 Hz, the second combined speeds for 18 Hz, 19 Hz and 20 Hz and the last combined speeds for all 15 Hz through 20 Hz. It is observed from Table 4, that the obtained estimates of the product of crack stiffness parameter and participation factor ($\Delta k_\xi p_i$) are maintaining consistency (the estimated parameters for all combined speeds lie between estimates of parameters for lower speeds range and higher speed range) except for 1X harmonic. And it is because of the bow and unbalance forces also lie on 1X harmonic. Even the bow effect was removed by slow roll rotor displacement, but still, it is affecting the estimates of the disc eccentricity and its phase. However, the consistency in estimates has been seen in the stationary damping and the rotating damping.

Table 4.

Estimated rotor parameters from experimental data

Parameters	15, 16 and 17 Hz combined speeds	18, 19 and 20 Hz combined speeds	15 through 20 Hz combined speeds
c_E (Nsm^{-1})	1291.9967	1775.0819	1377.2959
c_H (Nsm^{-1})	483.5822	311.0272	418.0876
e (10^{-4} m)	10.1009	8.3721	1.8464
ϕ (deg)	173.4	-179.3	176.2
$\Delta k_\xi p_0$	-11987.0984	-9913.9144	-9434.5097
$\Delta k_\xi p_1$	231606.6802	276027.9744	-8341.9619
$\Delta k_\xi p_2$	-65026.7530	-88689.1288	-70677.4922
$\Delta k_\xi p_3$	29917.1322	68000.1890	43761.9400
$\Delta k_\xi p_5$	-44649.7133	-31458.0987	-34736.0346
$\Delta k_\xi p_7$	-16868.7076	-23160.3580	-18251.1669
$\Delta k_\xi p_{-1}$	-285337.2953	-341353.1149	-304201.2771
$\Delta k_\xi p_{-3}$	11526.3482	38653.1516	23014.2936
$\Delta k_\xi p_{-5}$	-9579.1544	-12701.7005	-10344.1239

7. Validation through numerical simulations

In this section, a numerical simulation has been done through MATLAB^{TM} Simulink model based on test rig configuration and estimated parameters through experimental responses provided in Tables 1 and 4. Herein, the Simulink model developed based on EOMs illustrated in Equation (2), and it generates time domain responses for different rotor speeds. The Simulink block for the proposed rotor system is developed. The simulation runs for 8 s duration to obtain responses and is considered for complete cycles (n) of the rotor rotation. The sampling time is kept the same as that used in experimentally acquired data.

The generated numerical responses are used to plot the orbit and are illustrated in Fig. 14 for the spin speed of 20 Hz. It compares well with the experimental orbit plot, as shown in Fig. 12b, for the spin speed 20 Hz. These responses are used to generate the full spectrum amplitudes for 20 Hz rotor speed and are shown in Fig. 15. Table 5 shows that the most of higher amplitudes are similar in the experimental and numerical full spectrum, as well as lower amplitudes for 20 Hz rotor speed. The similarity in the orbit and the full spectrum amplitudes from experimental data and numerical generated data validates the identification algorithm.
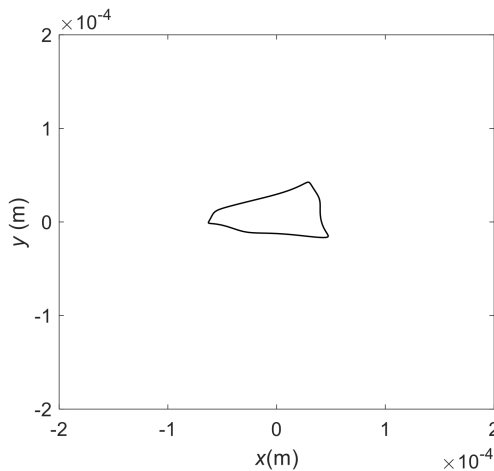

Fig. 14. Orbit plot x vs. y through Simulink at 20 Hz
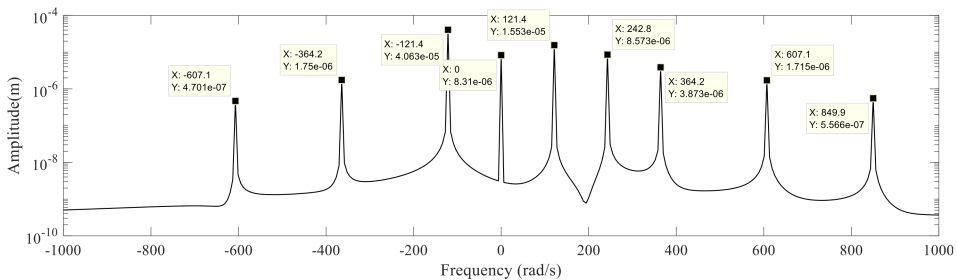

Fig. 15. Full spectrum response through Simulink (numerical) at 20 Hz

The identified multiple participation factor and crack stiffness product parameter ($\Delta k_\xi p_i$) are illustrated in Table 4. It is used to produce the crack force according to Equation (6) after dynamic condensation, i.e., on elimination of the slave part, as is given in Fig. 16. In Fig. 16, the full spectrum of the crack force for 20 Hz rotor speed is shown by using of the identified $\Delta k_\xi p_i$ for combined speeds (15 through 20 Hz).

Table 5.

Validation amplitudes at different harmonics of full spectrum at 20 Hz rotor spin speed

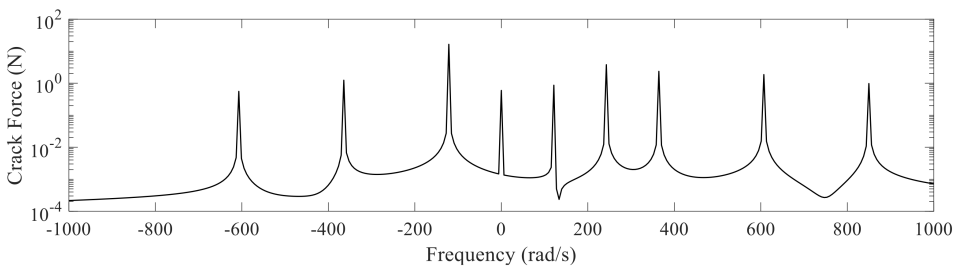| Frequency	Experimental (10^{-5} m)	Simulation (10^{-5} m)	Frequency	Experimental (10^{-5} m)	Simulation (10^{-5} m)
0	1.1408	0.8310	7ω	0.0861	0.0557
ω	1.3679	1.5526	$-\omega$	4.6157	4.0634
2ω	0.9997	0.8573	-3ω	0.4658	0.1750
3ω	0.6361	0.3873	-5ω	0.0549	0.0470
5ω	0.4044	0.1715			

Fig. 16. Crack force response at 20 Hz

8. Conclusions

The main goal of the present work is the experimental identification of the rotating and stationary damping with the help of a rotor model. The existence of rotating damping is considered only at the crack portion of rotor shaft and the rotor speed much below the critical speed ensure negligibly small material rotating damping and from other portion of the rotor shaft. Apart from the damping, the unbalance and the product of crack and participation factor were also estimated. The full spectrum is obtained through the regression-based and FFT-based methodology, and both compares well after the phase compensations, which uses a multi-frequency phase reference signal from the motor shaft. The shaft bow and sensor gap effects were removed through full spectrum vectors (complex) using the slow run full spectrum vectors. Then, the estimated parameters are used in equations of motion of rotor test setup configuration and through numerical simulation with Simulink block the displacement responses are generated. These displacement responses are compared with experimental responses in the form of orbits and full spectrum for validation of the identification methodology and overall rotor modeling. The novelty of this work is that it gives as an idea of rotating damping from the crack and it identifies experimentally along with stationary damping and other parameters of the cracked rotor system. It also supports in the generation of the periodic crack force, from which a newer crack model can be envisioned.

The present work can be extended with the finite element modeling considering shaft inertia and bearing flexibility to cater more practical rotor system.

A. Appendix: system matrices and vectors

The details of the matrices and vectors, mentioned in Equation (1), are given as

$$
\mathbf{M} = \begin{bmatrix} m & 0 & 0 & 0 \\ & m & 0 & 0 \\ & & I_d & 0 \\ \text{sym} & & & I_d \end{bmatrix}, \quad
\mathbf{C}_E = \begin{bmatrix} c_{22} & 0 & c_{24} & 0 \\ 0 & c_{33} & 0 & c_{35} \\ c_{42} & 0 & c_{44} & 0 \\ 0 & c_{53} & 0 & c_{55} \end{bmatrix},
$$

$$
\mathbf{K} = \begin{bmatrix} k_{22} & 0 & k_{24} & 0 \\ & k_{33} & 0 & k_{35} \\ & & k_{44} & 0 \\ \text{sym} & & & k_{55} \end{bmatrix}, \quad
\mathbf{G} = \begin{bmatrix} 0 & 0 & 0 & 0 \\ 0 & 0 & 0 & 0 \\ 0 & 0 & 0 & I_p \\ 0 & 0 & -I_p & 0 \end{bmatrix},
$$

$$
\mathbf{C}_E = \begin{bmatrix} c_E & 0 & 0 & 0 \\ 0 & c_E & 0 & 0 \\ 0 & 0 & 0 & 0 \\ 0 & 0 & 0 & 0 \end{bmatrix}, \quad
\mathbf{C}_H = \begin{bmatrix} c_H & 0 & 0 & 0 \\ 0 & c_H & 0 & 0 \\ 0 & 0 & 0 & 0 \\ 0 & 0 & 0 & 0 \end{bmatrix}, \tag{A.1}
$$

$$
\mathbf{C}_{1H} = \begin{bmatrix} 0 & c_H & 0 & 0 \\ -c_H & 0 & 0 & 0 \\ 0 & 0 & 0 & 0 \\ 0 & 0 & 0 & 0 \end{bmatrix}, \quad
\mathbf{f}_{cr}(t) = \frac{1}{2}\sigma(t) \begin{Bmatrix} \Delta k_{22}(1 + \cos 2\omega t)u_{x0} \\ \Delta k_{22} \sin(2\omega t)u_{x0} \\ \Delta k_{44}(1 + \cos 2\omega t)\varphi_{y0} \\ \Delta k_{44} \sin(2\omega t)\varphi_{y0} \end{Bmatrix},
$$

$$
\mathbf{f}_{unb} = \begin{Bmatrix} me\omega^2 \cos(\omega t + \phi) \\ me\omega^2 \sin(\omega t + \phi) \\ 0 \\ 0 \end{Bmatrix}, \quad
\mathbf{f}_{st} = \begin{Bmatrix} mg \\ 0 \\ 0 \\ 0 \end{Bmatrix}, \quad
\mathbf{q} = \begin{Bmatrix} x \\ y \\ \varphi_y \\ \varphi_x \end{Bmatrix} \quad \text{and} \quad \mathbf{q} = \mathbf{q}_v + \mathbf{q}_0.
$$

The static deflection force, $\mathbf{f}_{st} = \mathbf{K}\,\mathbf{q}_0$, is given as

$$
\begin{Bmatrix} mg \\ 0 \\ 0 \\ 0 \end{Bmatrix} = \begin{bmatrix} k_{22} & 0 & k_{24} & 0 \\ & k_{33} & 0 & k_{35} \\ & & k_{44} & 0 \\ \text{sym} & & & k_{55} \end{bmatrix} \begin{Bmatrix} u_{x0} \\ u_{y0} \\ \varphi_{y0} \\ \varphi_{x0} \end{Bmatrix}.
$$

After expanding the above matrix, we get

$$
\left.\begin{aligned}
u_{x0} &= \frac{mgk_{44}}{k_{44}k_{22} - k_{24}^2} \\
u_{y0} &= 0, \quad \varphi_{x0} = 0 \\
\varphi_{y0} &= \frac{mgk_{24}}{k_{24}^2 - k_{44}k_{22}}
\end{aligned}\right\} \quad \text{and} \quad \mathbf{q}(t)\mathbf{q} = \mathbf{q}_v(t) + \mathbf{q_0} \quad \text{where,}
$$

$$
\mathbf{q}_v(t) = \left\{ \begin{array}{c} u_x(t) \\ u_y(t) \\ \varphi_y(t) \\ \varphi_x(t) \end{array} \right\} \quad \text{and} \quad \mathbf{q_0} = \left\{ \begin{array}{c} u_{x0} \\ 0 \\ \varphi_{y0} \\ 0 \end{array} \right\}.
$$

The details of the vectors and matrices, mentioned in Equation (11), are given as

$$
\mathbf{A}_{1_{n\times9}}(t) = \begin{bmatrix}
1 & e^{j\omega t_1} & e^{j2\omega t_1} & e^{j3\omega t_1} & e^{j5\omega t_1} & e^{j7\omega t_1} & e^{-j\omega t_1} & e^{-j3\omega t_1} & e^{-j5\omega t_1} \\
1 & e^{j\omega t_2} & e^{j2\omega t_2} & e^{j3\omega t_2} & e^{j5\omega t_2} & e^{j7\omega t_2} & e^{-j\omega t_2} & e^{-j3\omega t_2} & e^{-j5\omega t_2} \\
\vdots & \vdots & \vdots & \vdots & \vdots & \vdots & \vdots & \vdots & \vdots \\
1 & e^{j\omega t_n} & e^{j2\omega t_n} & e^{j3\omega t_n} & e^{j5\omega t_n} & e^{j7\omega t_n} & e^{-j\omega t_n} & e^{-j3\omega t_n} & e^{-j5\omega t_n}
\end{bmatrix},
$$

$$
\bar{\mathbf{V}}_{i_{9\times1}} = \begin{bmatrix} \bar{\mathbf{v}}_0 & \bar{\mathbf{v}}_1 & \bar{\mathbf{v}}_2 & \bar{\mathbf{v}}_3 & \bar{\mathbf{v}}_5 & \bar{\mathbf{v}}_7 & \bar{\mathbf{v}}_{-1} & \bar{\mathbf{v}}_{-3} & \bar{\mathbf{v}}_{-5} \end{bmatrix}^T \quad \text{and} \tag{A.2}
$$

$$
\mathbf{v}_{n\times1}(t) = \begin{bmatrix} \mathbf{v}(t_1) & \mathbf{v}(t_2) & \cdots & \mathbf{v}(t_n) \end{bmatrix}.
$$

Details of the matrices and vectors mentioned in equation (14) are given as

$$
\begin{aligned}
&\begin{bmatrix} \mathbf{M}_{mm} & 0 \\ 0 & \mathbf{M}_{ss} \end{bmatrix} = \begin{bmatrix} m & 0 \\ 0 & I_d \end{bmatrix}, \quad
\begin{bmatrix} \mathbf{C}_{mm} & \mathbf{C}_{ms} \\ \mathbf{C}_{sm} & \mathbf{C}_{ss} \end{bmatrix} = \begin{bmatrix} c_E & 0 \\ 0 & 0 \end{bmatrix}, \\
&\begin{bmatrix} 0 & 0 \\ 0 & \mathbf{G}_{ss} \end{bmatrix} = \begin{bmatrix} 0 & 0 \\ 0 & -I_p \end{bmatrix}, \quad
\begin{bmatrix} \mathbf{K}_{mm} & \mathbf{K}_{ms} \\ \mathbf{K}_{sm} & \mathbf{K}_{ss} \end{bmatrix} = \begin{bmatrix} k_{22} & k_{23} \\ k_{32} & k_{33} \end{bmatrix}, \\
&\begin{bmatrix} \mathbf{C}_{Hmm} & 0 \\ 0 & 0 \end{bmatrix} = \begin{bmatrix} c_H & 0 \\ 0 & 0 \end{bmatrix}, \quad
\left\{ \begin{array}{c} \mathbf{q}_{mm} \\ \mathbf{q}_{ss} \end{array} \right\} = \left\{ \begin{array}{c} \mathbf{R}_i \\ \mathbf{\Phi}_i \end{array} \right\} \quad \text{and}
\end{aligned} \tag{A.3}
$$

$$
\left\{ \begin{array}{c} \mathbf{f}_i \\ \mathbf{0} \end{array} \right\} = \left\{ \begin{array}{c} \Delta K_{22}u_{x0} \sum\limits_{i=-n}^{i=n} p_i \\ 0 \end{array} \right\} + \left\{ \begin{array}{c} me\omega^2 e^{j\phi} \\ 0 \end{array} \right\}_{i=1} + \left\{ \begin{array}{c} \omega c_H u_{x0} e^{j\pi/2} \\ 0 \end{array} \right\}_{i=0}.
$$

On application of condensation, the reduced form of matrices and vectors, for Equation (18), are given as

$$\mathbf{M}^D = \left(\mathbf{T}^D\right)^T \begin{bmatrix} \mathbf{M}_{mm} & \mathbf{0} \\ \mathbf{0} & \mathbf{M}_{ss} \end{bmatrix} \mathbf{T}^D = \begin{bmatrix} m + \left(t_i^d\right)^2 I_d & 0 \\ 0 & m + \left(t_i^d\right)^2 I_d \end{bmatrix}, \quad \text{(A.4)}$$

$$\mathbf{K}^D = \left(\mathbf{T}_i^D\right)^T \begin{bmatrix} \mathbf{k}_{mm} & \mathbf{k}_{ms} \\ \mathbf{k}_{sm} & \mathbf{k}_{ss} \end{bmatrix} \mathbf{T}_i^D$$
$$= \begin{bmatrix} k_{22} + 2t_i^d k_{24} + \left(t_i^d\right)^2 k_{44} & 0 \\ 0 & k_{22} + 2t_i^d k_{24} + \left(t_i^d\right)^2 k_{44} \end{bmatrix}, \quad \text{(A.5)}$$

$$\mathbf{c}^D = \left(\mathbf{T}_i^D\right)^T \begin{bmatrix} \mathbf{c}_{mm} & \mathbf{c}_{ms} \\ \mathbf{c}_{sm} & \mathbf{c}_{ss} \end{bmatrix} \mathbf{T}_i^D = \begin{bmatrix} c_E & 0 \\ 0 & c_E \end{bmatrix}, \quad \text{(A.6)}$$

$$\mathbf{c}_H^D = \left(\mathbf{T}_i^D\right)^T \begin{bmatrix} \mathbf{c}_{H_{mm}} & 0 \\ 0 & 0 \end{bmatrix} \mathbf{T}_i^D = \begin{bmatrix} c_H & 0 \\ 0 & c_H \end{bmatrix}, \quad \text{(A.7)}$$

$$\mathbf{G}^D = \left(\mathbf{T}_i^D\right)^T \begin{bmatrix} \mathbf{0} & \mathbf{0} \\ \mathbf{0} & \mathbf{G}_{ss} \end{bmatrix} \mathbf{T}_i^D = \begin{bmatrix} -I_p \left(t_i^d\right)^2 & 0 \\ 0 & -I_p \left(t_i^d\right)^2 \end{bmatrix}, \quad \text{(A.8)}$$

$$\mathbf{f}^D = \left(\mathbf{T}_i^D\right)^T \begin{Bmatrix} \mathbf{f}_m \\ \mathbf{f}_s \end{Bmatrix} = \begin{Bmatrix} me\omega^2 \cos(\phi) \\ me\omega^2 \sin(\phi) \end{Bmatrix} + \begin{Bmatrix} (\Delta k_{22} u_{x0}) \, p_i \\ 0 \end{Bmatrix}$$
$$- \omega \begin{Bmatrix} 0 \\ -c_H u_{x0} \end{Bmatrix}. \quad \text{(A.9)}$$

The details of the remaining matrices and vectors, mentioned in Equation (22), are given as

$$\mathbf{x} = \begin{bmatrix} c_E & c_H & e_{\text{Re}} & e_{\text{Im}} & -p_0 & -p_1 & -p_2 & -p_3 & -p_5 & -p_7 & -p_{-1} & -p_{-3} & -p_{-5} \end{bmatrix}^T,$$

$$\mathbf{b} = \begin{Bmatrix} b_1 & b_2 & b_3 & b_4 & b_5 & b_6 & b_7 & b_8 & b_9 & b_{10} & b_{11} & b_{12} & b_{13} & b_{14} & b_{15} & b_{16} & b_{17} & b_{18} \end{Bmatrix}^T,$$

$$b_1 = -k_0 R_{0_{\text{Re}}}, \quad b_2 = \left(\omega^2 m_1 + \omega^2 I_p \left(t_1^d\right)^2 - k_1\right) R_{1_{\text{Re}}},$$

$$b_3 = \left(4\omega^2 m_2 + 2\omega^2 I_p \left(t_2^d\right)^2 - k_2\right) R_{2_{\text{Re}}},$$

$$b_4 = \left(9\omega^2 m_3 + 3\omega^2 I_p \left(t_3^d\right)^2 - k_3\right) R_{3_{\text{Re}}},$$

$$b_5 = \left(25\omega^2 m_5 + 5\omega^2 I_p \left(t_5^d\right)^2 - k_5\right) R_{5_{\text{Re}}},$$

$$b_6 = \left(49\omega^2 m_7 + 7\omega^2 I_p \left(t_7^d\right)^2 - k_7\right) R_{7_{\text{Re}}},$$

$$b_7 = \left(\omega^2 m_{-1} - \omega^2 I_p \left(t_{-1}^d \right)^2 - k_{-1} \right) R_{-1_{\mathrm{Re}}},$$

$$b_8 = \left(9\omega^2 m_{-3} - 3\omega^2 I_p \left(t_{-3}^d \right)^2 - k_{-3} \right) R_{-3_{\mathrm{Re}}},$$

$$b_9 = \left(25\omega^2 m_{-5} - 5\omega^2 I_p \left(t_{-5}^d \right)^2 - k_{-5} \right) R_{-5_{\mathrm{Re}}}, \quad b_{10} = -k_0 R_{0_{\mathrm{Im}}},$$

$$b_{11} = \left(\omega^2 m_1 + \omega^2 I_p \left(t_1^d \right)^2 - k_1 \right) R_{1_{\mathrm{Im}}},$$

$$b_{12} = \left(4\omega^2 m_2 + 2\omega^2 I_p \left(t_2^d \right)^2 - k_2 \right) R_{2_{\mathrm{Im}}},$$

$$b_{13} = \left(9\omega^2 m_3 + 3\omega^2 I_p \left(t_3^d \right)^2 - k_3 \right) R_{3_{\mathrm{Im}}},$$

$$b_{14} = \left(25\omega^2 m_5 + 5\omega^2 I_p \left(t_5^d \right)^2 - k_5 \right) R_{5_{\mathrm{Im}}},$$

$$b_{15} = \left(49\omega^2 m_7 + 7\omega^2 I_p \left(t_7^d \right)^2 - k_7 \right) R_{7_{\mathrm{Im}}},$$

$$b_{16} = \left(\omega^2 m_{-1} - \omega^2 I_p \left(t_{-1}^d \right)^2 - k_{-1} \right) R_{-1_{\mathrm{Im}}},$$

$$b_{17} = \left(9\omega^2 m_{-3} - 3\omega^2 I_p \left(t_{-3}^d \right)^2 - k_{-3} \right) R_{-3_{\mathrm{Im}}},$$

$$b_{18} = \left(25\omega^2 m_{-5} - 5\omega^2 I_p \left(t_{-5}^d \right)^2 - k_{-5} \right) R_{-5_{\mathrm{Im}}},$$

$$\mathbf{A} = \begin{bmatrix}
0 & \omega R_{0_{\mathrm{Im}}} & 0 & 0 & u_{x0} & 0 & 0 & 0 & 0 & 0 & 0 & 0 & 0 \\
-\omega R_{1_{\mathrm{Im}}} & 0 & -m\omega^2 & 0 & 0 & u_{x0} & 0 & 0 & 0 & 0 & 0 & 0 & 0 \\
-2\omega R_{2_{\mathrm{Im}}} & -\omega R_{1_{\mathrm{Im}}} & 0 & 0 & 0 & 0 & u_{x0} & 0 & 0 & 0 & 0 & 0 & 0 \\
-3\omega R_{3_{\mathrm{Im}}} & -2\omega R_{3_{\mathrm{Im}}} & 0 & 0 & 0 & 0 & 0 & u_{x0} & 0 & 0 & 0 & 0 & 0 \\
-5\omega R_{5_{\mathrm{Im}}} & -4\omega R_{5_{\mathrm{Im}}} & 0 & 0 & 0 & 0 & 0 & 0 & u_{x0} & 0 & 0 & 0 & 0 \\
-7\omega R_{7_{\mathrm{Im}}} & -6\omega R_{7_{\mathrm{Im}}} & 0 & 0 & 0 & 0 & 0 & 0 & 0 & u_{x0} & 0 & 0 & 0 \\
\omega R_{-1_{\mathrm{Im}}} & 2\omega R_{-1_{\mathrm{Im}}} & 0 & 0 & 0 & 0 & 0 & 0 & 0 & 0 & u_{x0} & 0 & 0 \\
3\omega R_{-3_{\mathrm{Im}}} & 4\omega R_{-3_{\mathrm{Im}}} & 0 & 0 & 0 & 0 & 0 & 0 & 0 & 0 & 0 & u_{x0} & 0 \\
5\omega R_{-5_{\mathrm{Im}}} & 6\omega R_{-5_{\mathrm{Im}}} & 0 & 0 & 0 & 0 & 0 & 0 & 0 & 0 & 0 & 0 & u_{x0} \\
0 & -\omega \left(R_{0_{\mathrm{Re}}} + u_{x0} \right) & 0 & 0 & 0 & 0 & 0 & 0 & 0 & 0 & 0 & 0 & 0 \\
\omega R_{1_{\mathrm{Re}}} & 0 & 0 & -m\omega^2 & 0 & 0 & 0 & 0 & 0 & 0 & 0 & 0 & 0 \\
2\omega R_{2_{\mathrm{Re}}} & \omega R_{2_{\mathrm{Re}}} & 0 & 0 & 0 & 0 & 0 & 0 & 0 & 0 & 0 & 0 & 0 \\
3\omega R_{3_{\mathrm{Re}}} & 2\omega R_{3_{\mathrm{Re}}} & 0 & 0 & 0 & 0 & 0 & 0 & 0 & 0 & 0 & 0 & 0 \\
5\omega R_{5_{\mathrm{Re}}} & 4\omega R_{5_{\mathrm{Re}}} & 0 & 0 & 0 & 0 & 0 & 0 & 0 & 0 & 0 & 0 & 0 \\
7\omega R_{7_{\mathrm{Re}}} & 6\omega R_{7_{\mathrm{Re}}} & 0 & 0 & 0 & 0 & 0 & 0 & 0 & 0 & 0 & 0 & 0 \\
-\omega R_{-1_{\mathrm{Re}}} & -2\omega R_{-1_{\mathrm{Re}}} & 0 & 0 & 0 & 0 & 0 & 0 & 0 & 0 & 0 & 0 & 0 \\
-3\omega R_{-3_{\mathrm{Re}}} & -4\omega R_{-3_{\mathrm{Re}}} & 0 & 0 & 0 & 0 & 0 & 0 & 0 & 0 & 0 & 0 & 0 \\
-5\omega R_{-5_{\mathrm{Re}}} & -6\omega R_{-5_{\mathrm{Re}}} & 0 & 0 & 0 & 0 & 0 & 0 & 0 & 0 & 0 & 0 & 0
\end{bmatrix}. \quad (A.10)$$

References

[1] R. Tiwari. *Rotor Systems: Analysis and Identification*. CRC Press, USA, 2017. doi: 10.1201/9781315230962.

[2] F. Ehrich. Shaft whirl induced by rotor internal damping. *Journal of Applied Mechanics*, 31(2):279–282, 1964. doi: 10.1115/1.3629598.

[3] L.-W. Chen and D.-M. Ku. Analysis of whirl speeds of rotor-bearing systems with internal damping by C^0 finite elements. *Finite Elements in Analysis and Design*, 9(2):169–176, 1991. doi: 10.1016/0168-874X(91)90059-8.

[4] D.-M. Ku. Finite element analysis of whirl speeds for rotor-bearing systems with internal damping. *Mechanical Systems and Signal Processing*, 12(5):599–610, 1998. doi: 10.1006/mssp.1998.0159.

[5] J. Melanson and J. Zu. Free vibration and stability analysis of internally damped rotating shafts with general boundary conditions. *Journal of Vibration and Acoustics*, 120(3):776–783, 1998. doi: 10.1115/1.2893897.

[6] G. Genta. On a persistent misunderstanding of the role of hysteretic damping in rotordynamics. *Journal of Vibration and Acoustics*, 126(3):459–461, 2004. doi: 10.1115/1.1759694.

[7] M. Dimentberg. Vibration of a rotating shaft with randomly varying internal damping. *Journal of Sound and Vibration*, 285(3):759–765, 2005. doi: 10.1016/j.jsv.2004.11.025.

[8] F. Vatta and A. Vigliani. Internal damping in rotating shafts. *Mechanism and Machine Theory*, 43(11):1376–1384, 2008. doi: 10.1016/j.mechmachtheory.2007.12.009.

[9] J. Fischer and J. Strackeljan. Stability analysis of high speed lab centrifuges considering internal damping in rotor-shaft joints. *Technische Mechanik*, 26(2):131–147, 2006.

[10] O. Montagnier and C. Hochard. Dynamic instability of supercritical driveshafts mounted on dissipative supports – effects of viscous and hysteretic internal damping. *Journal of Sound and Vibration*, 305(3):378–400, 2007. doi: 10.1016/j.jsv.2007.03.061.

[11] M. Chouksey, J.K. Dutt, and S.V. Modak. Modal analysis of rotor-shaft system under the influence of rotor-shaft material damping and fluid film forces. *Mechanism and Machine Theory*, 48:81–93, 2012. doi: 10.1016/j.mechmachtheory.2011.09.001.

[12] P. Goldman and A. Muszynska. Application of full spectrum to rotating machinery diagnostics. *Orbit*, 20(1):17–21, 1991.

[13] R. Tiwari. Conditioning of regression matrices for simultaneous estimation of the residual unbalance and bearing dynamic parameters. *Mechanical Systems and Signal Processing*, 19(5):1082–1095, 2005. doi: 10.1016/j.ymssp.2004.09.005.

[14] I. Mayes and W. Davies. Analysis of the response of a multi-rotor-bearing system containing a transverse crack in a rotor. *Journal of Vibration, Acoustics, Stress, and Reliability in Design*, 106(1):139–145, 1984. doi: 10.1115/1.3269142.

[15] R. Gasch. Dynamic behaviour of the Laval rotor with a transverse crack. *Mechanical Systems and Signal Processing*, 22(4):790–804, 2008. doi: 10.1016/j.ymssp.2007.11.023.

[16] M. Karthikeyan, R. Tiwari, S. and Talukdar. Development of a technique to locate and quantify a crack in a beam based on modal parameters. *Journal of Vibration and Acoustics*, 129(3):390–395, 2007. doi: 10.1115/1.2424981.

[17] S.K. Singh and R. Tiwari. Identification of a multi-crack in a shaft system using transverse frequency response functions. *Mechanism and Machine Theory*, 45(12):1813–1827, 2010. doi: 10.1016/j.mechmachtheory.2010.08.007.

[18] C. Shravankumar and R. Tiwari. Identification of stiffness and periodic excitation forces of a transverse switching crack in a Laval rotor. *Fatigue & Fracture of Engineering Materials & Structures*, 36(3):254–269, 2013. doi: 10.1111/j.1460-2695.2012.01718.x.

[19] S. Singh and R. Tiwari. Model-based fatigue crack identification in rotors integrated with active magnetic bearings. *Journal of Vibration and Control*, 23(6):980–1000, 2017. doi: 10.1177/1077546315587146.

[20] S. Singh and R. Tiwari. Model-based switching-crack identification in a Jeffcott rotor with an offset disk integrated with an active magnetic bearing. *Journal of Dynamic Systems, Measurement, and Control*, 138(3):031006, 2016. doi: 10.1115/1.4032292.

[21] S. Singh and R. Tiwari. Model based identification of crack and bearing dynamic parameters in flexible rotor systems supported with an auxiliary active magnetic bearing. *Mechanism and Machine Theory*, 122: 292–307, 2018. doi: 10.1016/j.mechmachtheory.2018.01.006.

[22] D.K. Roy, and R. Tiwari. Development of identification procedure for the internal and external damping in a cracked rotor system undergoing forward and backward whirls. *Archive of Mechanical Engineering*, 66(2):229–255. doi: 10.24425/ame.2019.128446.

[23] M. G. Maalouf. Slow speed vibration signal analysis: if you can't do it slow, you can't do it fast. In *Proceedings of the ASME Turbo Expo 2007: Power for Land, Sea, and Air*, volume 5, pages 559–567. Montreal, Canada, 14–17 May, 2007. doi: 10.1115/GT2007-28252.

[24] C. Shravankumar, R. Tiwari, and A. Mahibalan. Experimental identification of rotor crack forces. In: *Proceedings of the 9th IFToMM International Conference on Rotor Dynamics*: pp. 361–371, 2015. doi: 10.1007/978-3-319-06590-8_28.